Journal of Power Sources 617 (2024) 234916

Contents lists available at ScienceDirect

Journal of Power Sources

journal homepage: www.elsevier.com/locate/jpowsour

Exploring thermal runaway propagation in Li-ion batteries through high-speed X-ray imaging and thermal analysis: Impact of cell chemistry and electrical connections

Matilda Fransson [a,c,*], Jonas Pfaff [b], Ludovic Broche [c], Mark Buckwell [a,e], Charlie Kirchner-Burles [a,f], Hamish T. Reid [a], Sebastian Schopferer [b], Alexander Rack [c], Donal P. Finegan [d], Paul R. Shearing [g,e,**]

[a] Department of Chemical Engineering, University College London, London, UK
[b] Fraunhofer Institute for High-Speed Dynamics, Ernst-Mach-Institut, EMI, Efringen-Kirchen, Germany
[c] ESRF – The European Synchrotron, Grenoble, France
[d] National Renewable Energy Laboratory, 15013 Denver W Parkway, Golden, CO 80401, USA
[e] The Faraday Institution, Harwell Science and Innovation Campus, Didcot, UK
[f] National Physical Laboratory, Teddington, Middlesex, TW11 0LW, UK
[g] Department of Engineering Science, University of Oxford, Parks Road, Oxford, OX 3PJ, UK

HIGHLIGHTS

- 56% chance of Li-ion battery failure propagation for abusive test scenarios conducted.
- Spatio-temporal mapping of Li-ion battery failure from High-Speed X-ray Imaging.
- Cell chemistry and electrical connection influence failure temperature and speed.

ARTICLE INFO

MSC:
0000
1111

Keywords:
Li-ion battery safety
Thermal runaway
Synchrotron
X-ray imaging

ABSTRACT

Battery safety design is important to consider from the individual Li-ion cell to the level of the macro-system. On the macro-level, failure in one single cell can lead to propagation of the thermal runaway and rapidly set a whole battery pack on fire. Factors that can impact the propagation outcome, such as cell model/chemistry and electrical connection are here investigated using a combination of measurements. Several abusive tests were conducted, combining two different cell models (Molicel P42A and LG M50, both 21700s) in series and parallel connections (16 tests per configuration). Overall, a propagation outcome of 56% was measured from the 32 conducted tests, a minimum temperature of 150 °C was required to initiate propagation, and the fastest propagation occurred in 123 s. Temperature measurements were higher in series connected cells, initiating the discussion of cell chemistry and internal resistance on this effect. The difference in current-flow during thermal runaway in series and parallel connections, and how this can affect the temperature evolution is further discussed. Spatio-temporal mapping of X-ray radiography allowed us to derive the speed of thermal runaway evolution inside the battery and has shown that series connected cells, in particular P42A, occur faster. It was further observed that deviant sidewall behaviors such as temperature-induced breaches and pressure-induced ruptures occurred in P42As only respective nail-penetrated cells only.

* Corresponding author at: Department of Chemical Engineering, University College London, London, UK.
** Corresponding author.
E-mail addresses: matilda.fransson.20@ucl.ac.uk (M. Fransson), paul.shearing@eng.ox.ac.uk (P.R. Shearing).

https://doi.org/10.1016/j.jpowsour.2024.234916
Received 18 March 2024; Received in revised form 9 June 2024; Accepted 14 June 2024
Available online 31 July 2024

1. Introduction

Over the last decade, the worldwide adoption of electric vehicles (EV) has continued to accelerate [1]. This rapid evolution has relied on substantial improvements in cell design, capacity increase, lifetime extension, optimized module and pack design, increased production efficiency, and improved cell and battery system management [2]. According to different estimations, this number is expected to reach 30–60 million global EV sales by 2030, with 60 million sales being the net zero emission scenario. In addition, in 2021 energy storage systems (ESS) reached a total of 16 GW, but in order to reach the net zero scenario, 680 GW are needed by 2030 [3]. The electrochemical properties of lithium-ion batteries (LiB) and their resulting high energy and power density provide ideal conditions for their use as effective energy storage. However, LiB design involves several engineering challenges spanning the material level to system level, where one of the major challenges is thermal and safety management. Whilst failure events are rare, previous LiB accidents in consumer electronics, electric vehicles, air crafts and grid-storage installations have drawn attention to their potential for aggressive and hazardous failures [4].

During failure events, the combination of high energy density and thermally unstable constituent materials can ignite multiple exothermic decomposition reactions that can result in an uncontrollable series of events known as thermal runaway (TR), which may lead to an explosion of the cell [5–8]. If the cell is mechanically or electrically damaged, for example through the intrusion of a metallic object or the formation of metallic dendrites, direct contact between anode and cathode can be established leading to a rapid discharge coupled with a temperature spike that may initiate the TR.

Faulty operation modes can locally increase the temperature of the cell, or an unexpected increase in the surrounding temperature may externally heat the battery to the point of TR initiation. Initially, around 80 °C, the solid electrolyte interphase (SEI) layer will start to decompose and generate gaseous products. At 90 °C the electrolyte evaporation will begin, leading to the additional gas formation that in turn can lead to internal stress due to the pressure increase [9]. Therefore, many commercial batteries have been equipped with safety vents that allow the cell to release the gaseous overpressure and decrease the internal temperature, preventing or mitigating a TR.

Between 100–200 °C, the separator begins to melt and exothermic breakdown of electrolyte salts initiates. Commercial cells are often equipped with a three-layered separator, where the middle layer is designed to melt once the critical temperature is reached and through this process block the ion-permeable pores. This charge-inhibiting protection mechanism is usually activated around 130 °C. Above 200 °C, the anode and cathode materials will exothermally decompose [9–11].

Considering the increased size and complexity of battery systems, a better understanding of the impact of one cell on the system is essential. It has previously been demonstrated that one single cell failure in multiple battery configurations can generate sufficient heat to initiate a TR in neighboring cells, that in a cascading manner can lead to catastrophic failures [4,12–15]. For this reason, battery module and pack safety systems are generally installed to prevent TR from propagating throughout the entire unit. Failure tests and increased understanding TR propagation is crucial for several reasons, not only to improve safety designs, but also for performance optimization, minimizing environmental damage and cost reduction. It is also essential that governmental safety standards and requirements are formulated appropriately.

TR is a well-studied phenomenon in the field of battery safety and in recent years, researchers have made significant progress in understanding the underlying mechanisms of TR and TR propagation. Heat transfer between connected cells is the main factor that has been identified as critical for the propagation of TR, however, studies have also shown that other parameters, such as the electrical connection between the cells also play a significant role in TR propagation. Lamb et al. [13] compared TR propagation of two different battery modules, 10s1p (10 batteries in series) and 1s10p (10 batteries in parallel) and found that propagation was more likely for the latter and concluded this was a result of ‘current dumping’. As the neighboring cell discharges through the trigger cell, this dumps its current in the already failed cell. Plunkett et al. [16] performed cell-to-cell propagation tests on 18650 and 21700 connected in parallel, at varying states of charge in order to estimate the magnitude of this ‘current dumping’. Their work led to the design of a current collector fuse. In another study, Liu et al. [17] observed intensified TR propagation in parallel connected modules.

In this work, for the first time, we have applied high-speed X-ray imaging with the aim of improving the understanding of cell-to-cell propagation between a pair of cylindrical cells with different electrical configurations. This work focuses on the real-time application of radiography to investigate the internal structural changes during abusive testing resulting in battery failure and TR propagation. This is directly relevant to cell engineering as it feeds into how original equipment manufacturers may consider design optimization for safety, based on what is happening within the cell, without necessarily requiring additional measurements to be conducted. The in-situ measurements could later be combined with ex-situ measurements like SEM or XRD for a more complete picture of the event. However this has already been demonstrated in previous studies [18] and is therefore considered out of the scope of this work.

Two cell models with different cathode chemistry were tested in situ, both in parallel and series configuration. High-speed X-ray imaging has previously successfully been combined with failure testing of LiB and given insights into how TRs are initiated and escalated. With these tests, we aim to establish a better understanding of the internal dynamics of the propagation phenomenon in relation to cell chemistry and electrical connection, to subsequently inspire development of precautionary mechanisms that can be implemented both in single cells and in module/pack configurations.

The X-ray field of view (FOV) was alternated between trigger and propagation cell, and allows a part of a single battery to be imaged at a given time. By altering the position of the FOV in-between tests we have been able to image TR in both trigger and propagating cells under replicated test conditions. Image processing techniques have afterwards allowed internal spatio-temporal mapping of the TR to in a second step determine the speed of the internal events. Additionally, we have obtained statistics of propagation, data for propagation time, temperature, heat rate and infrared images that we aim to discuss in relation to the image findings. The combination of several techniques and the resulting richness of data allows a deeper insight to the interdependence of parameters.

2. Experimental setup

Battery safety testing requires a controlled enclosure and environment, as well as rigorous safety measures to be put into place. In this work, we perform abusive tests of batteries in different electrical configurations using ’triggers’ to initiate battery failure; whilst these tests fall outside of the safe operational envelope of the cells under test, they provide a useful tool to explore the cells’ response to abusive conditions. To perform tests under such requirements in combination with synchrotron high-speed X-ray imaging, a specialized test chamber has been developed by the same research team [19], see setup in Figure 9 in Supplementary Materials. The high photon flux and high-energy X-rays are the key components available at the synchrotron that allows imaging of fast phenomena (such as the TR) on industrial scale samples containing highly attenuating materials. The experiments were conducted at a high-speed imaging specialized beamline (ID19) at the European Synchrotron Radiation Facility (ESRF), France. The chamber enables controlled investigation of battery failures, through externally induced TR (heating or nail penetration), along with coupling and synchronization of complementary measurement techniques such as

temperature, voltage and infrared imaging. To limit the severity of the failure and protect the chamber, a 15% CO_2 ratio was used for fire retention. For cell-to-cell propagation testing, a special cell holder that allows stacking of cells was utilized. Radiography acquisition and alignment is enabled through X-ray transparent aluminum windows and a flexible sample table.

The intense photon flux density at ID19 enables a high spatial resolution to be achieved. The acquisition scheme is based on an indirect X-ray image detector using SA-Z Photron (based on a CMOS-camera) with 5 kHz frame rate, lens-coupled to a LuAG:Ce scintillator screen. A beam energy of 85 keV was utilized and the propagation distance was set to 8 m. Optical lenses (100/100 Hasselblad, 1×) where connected in a tandem configuration for lens-coupling, yielding the native standard 20 μm pixel size of the camera. The pixel matrix of the detector is 1024 × 504 (region of interest set to match the beam size at the give photon energy), resulting in an approximate field-of-view (FoV) of 20 × 10 mm^2. For more details about the chamber and acquisition parameters we refer to the previously published work [19].

In this work, two commercially available cell models were studied: Molicel INR21700 P42 A, 4200 mAh (NCA chemistry) and LG INR21700 M50 (NMC chemistry). Here, 8 tests involved 2 cells in parallel-configuration pairs and 8 tests involved 2 cells in serial configuration, per cell model respectively, resulting in a total of 32 tests. The cells were placed directly in contact with each other as in Figure 9(b) in Supplementary Materials. The position of the X-ray FoV was alternated between the trigger and propagation cell resulting in 4 nominally identical tests in each cell and image configuration. The cells were aligned horizontally within the cell holder [20] according to the desired configuration, and electrically connected via welded cell tabs. The wires for the voltage reading were welded onto the tabs. Thermocouples were fastened in the middle of the cell surface using Kapton tape and heat conductive glue. Each cell was coated with black carbon paint to reduce reflectivity and improve the quality of the thermal images. The trigger cell was penetrated around the center with a speed of 6 mm s^{-1} to an approximate depth of 1–3 mm, and propagation awaited.

Labeling of experiments in this work has been done as following: 'PT' stands for 'Parallel Trigger', meaning the cells are connected in parallel and the X-ray FoV cover the trigger cell, accordingly 'PP' refers to parallel connection with X-ray FoV covering the propagating cell. Similarly, 'ST' and 'SP' stands for series connection, with the same labeling as above for X-ray FoV.

3. Data processing

The temperature data obtained from thermocouple sensors allow comparisons of both maximum temperatures and the temperature distribution over time, thus allowing conclusions to be drawn about the propagation behavior of the cells. Average and standard deviation (std) is calculated for each group of data presented. The std is calculated using the "n-1" method as demonstrated in Eq. (1) below:

$$std = \sqrt{\frac{\sum_{i=1}^{n}(x_i - \bar{x})^2}{n-1}} \tag{1}$$

3.1. Heat distribution

From acquired temperature data, heat rates were calculated to increase the understanding of the propagation phenomenon. To illustrate this data processing, temperature curves of two experiments are plotted as examples in Figure 10 in Supplementary Materials. The subfigures represent one experiment in which propagation took place (a:'M50_PT_Exp4') and one experiment without propagation (b:'M50_PP_Exp3'). The temperature curves illustrate the representative temperature behavior of TR and can be categorized in 'sections' as subsequently described. During the immediate TR initiation and reactions following nail penetration, the measured temperature rises rapidly over 600 °C in both cases. The high reproducibility (due to the defined triggering of the TR) allows comparison of all temperature curves for all trigger cell tests. The time between the temperature increase caused by the TR of the cell and the maximum measured temperature is classified as Section 1. Subsequently, the trigger cell starts to cool down and the dissipated heat is conducted to the propagation cell that heats up. This temporal range, between TR of the first cell and possible TR of the second cell, is crucial for understanding propagation behavior of the studied configurations. For this reason, further analyses are mainly focused on the temperature curves within this range (see Section 2). The end of this section is specified according to the temperature of the propagating cell. For experiments with propagation, the second section ends at the onset of the TR in the second cells, while for experiments without propagation, this section ends at the temperature maximum of the propagation cell, after which the temperature slowly cools down again (Figure 10 in Supplementary Materials). Section 3 contains the TR temperature response of the second cell. For this reason, this section is not represented in experiments without propagation. Section 4 marks the cooling behavior after both cells failed or no propagation reaction can be assumed from the second cell anymore. The presented ΔT values in Figure 1 in Supplementary Materials represents the average temperature changes within the corresponding section.

3.2. Velocity

To compute the longitudinal velocity of the electrode's layers delamination during TR the following image processing pipeline was developed (Fig. 1). All image processing algorithms were implemented in python3.8 using the itk and sklearn library [21]. First, every radiography was flat-field corrected to remove any artifacts or inhomogeneities from the synchrotron X-ray source. The electrode layers were then extracted using a Gabor filtering technique developed by A.Radhakrishnan and M.Buckwell [22]. In summary, a Gabor transform was applied to every image, decomposing it into a series of localized and oriented wavelets at various spatial frequencies. The layers were then extracted by filtering in the horizontal wavelets matching the electrodes thickness (Fig. 1). To have a representation of the delamination evolution, a spatio-temporal cross-correlation was applied to the segmented layers at every time point, a similar approach was used by A.Radhakrishnan and M.Buckwell [22]. To do so, every vertical cross section (pixel column) at each time point was compared to its respective column at (first frame of the recording) by calculating the cross-correlation. In the output cross-correlation image, a correlation close to 1 represents at a given horizontal position a similarity of structure between time t_0 and t. Horizontal movement of layers then has fringes of strong positive correlation value (close to 1), for which their slope is direct measurement of their velocity (Fig. 1). To compute the velocity of layers, the cross-correlation fringes were then extracted by applying a threshold between 0.7 and 1 (for necessary noise filtering) and thereafter labeled (Fig. 1). In regions where neither strong positive or negative correlation can be found, the color-map contains no useful information. Therefore the regions of interest were selected to frame the parts of the correlation map where the patterns are most distinguishable for speed retrieval. A morphological skeleton operation was then applied to extract their main orientation. Finally, an iterative linear regression was applied to every skeleton to compute their respective velocity. If the regression mean square error was too large, the skeleton was then recursively cut in two segments until proper fitting.

With this technique, each TR radiography recording (trigger and propagation events) are 'speed-mapped' and the estimated speeds thereafter constitutes a comparison parameter for understanding the TR evolution in the different cell configurations (trigger/propagation cell, P42A/M50, series/parallel). Statistical evidence within speed data groups and values are examined using the non-parametric statistical Mann–Whitney U test, suitable for data distributions found in this work, using the SPSS software version 29.

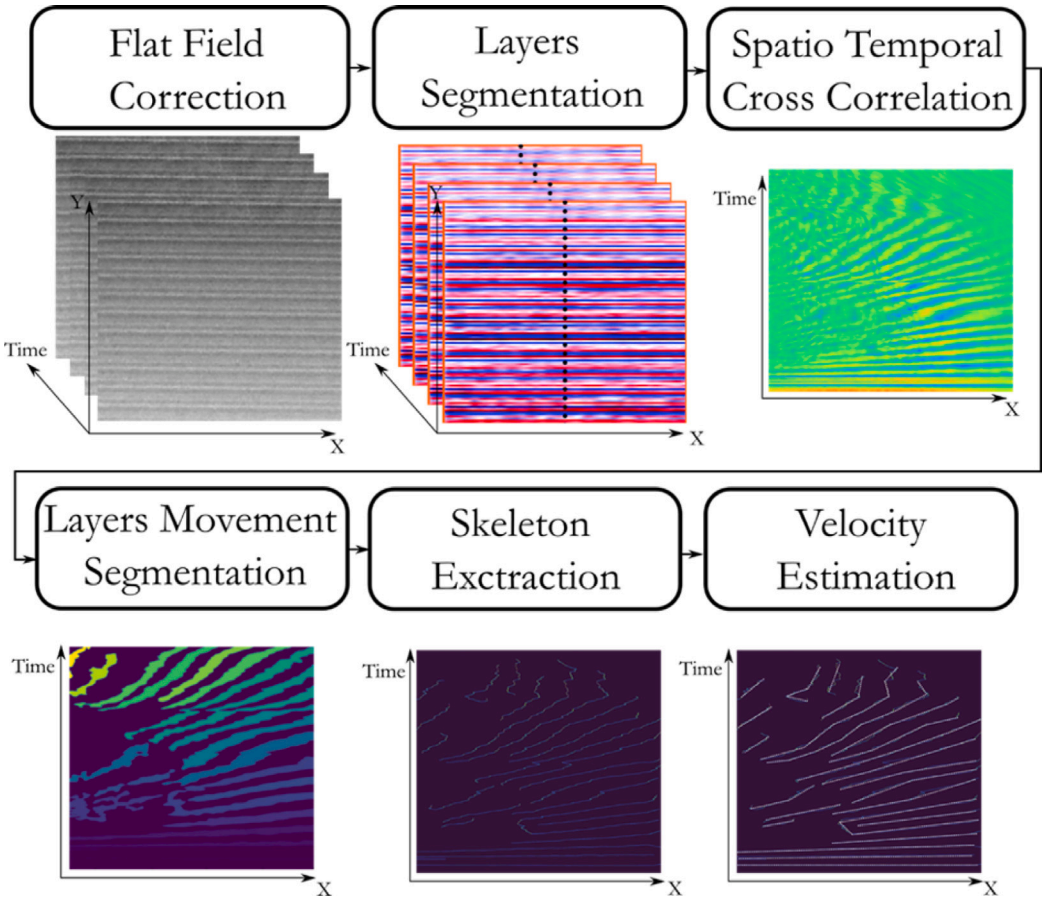

Fig. 1. Graphic illustration of the speed derivation process from the Flat-Field Corrected X-ray Images. In the first processing step, segmentation of the electrode layers is achieved by applying Gabor filtering and is followed by spatio-temporal cross-correlation of these filtered frames. The lines appearing from correlation and decorrelation variations are related to the delamination of the electrode layers. In the following step, the 'movement-pattern' segments of the speed map have been extracted and separately labeled. Subsequently, the center line for each segment (skeleton) has been extracted. In the following analysis step, linear regression is applied to the line segments in to retrieve the speed of the TR.

4. Results and discussion

In total, 32 propagation experiments were conducted and in 18 of the tests (56%), cell-to-cell propagation occurred. The propagation outcome can be determined by the temperature spikes in the thermocouple readings, where only one spike is present if no propagation occurred and two spikes visible if propagation occurred. The propagation outcomes are distributed over the different configurations and cell models as presented in Tables 1–4 in the 'Propagation' column, showing no significant trend towards the propagation outcome depending on cell model nor the different electrical connections.

All nail penetration failures and 10 propagation events were captured with X-ray imaging. The failures have during analysis been classified into 4 different groups based on collected X-ray radiography, as listed below and further demonstrated in Fig. 2. Each TR event exhibits different behaviors, however, the classification below is based on the visual similarities and/or the final outcome, which in this case refers to sidewall behaviors such as melt and ruptures. This visual grouping of experiments simplifies the presentation and discussion of all collected data.

(1) Quintessential representation of nail penetration failures in trigger cells

(2) Quintessential representation of failure in propagating cells

(3) Representation of sidewall melting in trigger and propagating cells

(4) Representation of sidewall rupture in trigger cell

Radiography category 1 represents the evolution of TR in nail penetrated cells. Here, cell disintegration is initiated to the left of the nail immediately after nail penetration and thereafter spreads throughout the cell with varying speeds. It is observed that layers are often disconnected from the jellyroll, while being pushed towards the venting region of the battery (to the left in the frame).

The second category represents propagation failures that all have similar failure behavior, where the layers are exhibiting more of a dissipation behavior, rather than disintegration as in Category 1. This difference is most likely related to the difference in failure initiation, where TR in category 2 are triggered by external heating and in category 1 instead by internal heat. Categories 3 and 4 include experiments where failure leads to sidewall melts and ruptures. However, the severity, location, and size of all sidewall breakages vary within the two categories. We distinguish between a melt and a rupture with the former being more temperature-dependent and the latter more pressure-dependent. Examples of the two sidewall categories are presented in Figure 11 in Supplementary Materials, where (a) shows a sidewall melt, (b) a sidewall rupture and (c) an example of a cell that moved within the FoV. In 4 of the M50 tests, the cell moved within the FoV and neither failure classification nor speed calculations were not possible. Failure classification shows that sidewall melts are only observed in P42As and sidewall ruptures are only observed in trigger cells, but no correlations to the measured temperatures are found. Sidewall melts only occurring in P42As could be explained by the cell chemistry, leading to higher temperatures close to the wall. Rupture only occured in trigger cells, where the rapid initiation will lead to a fast accumulation of gas and this will limit the time for safety vents to activate. The TR being initiated to the left of the nail could also lead to material clogging the vent in trigger cells.

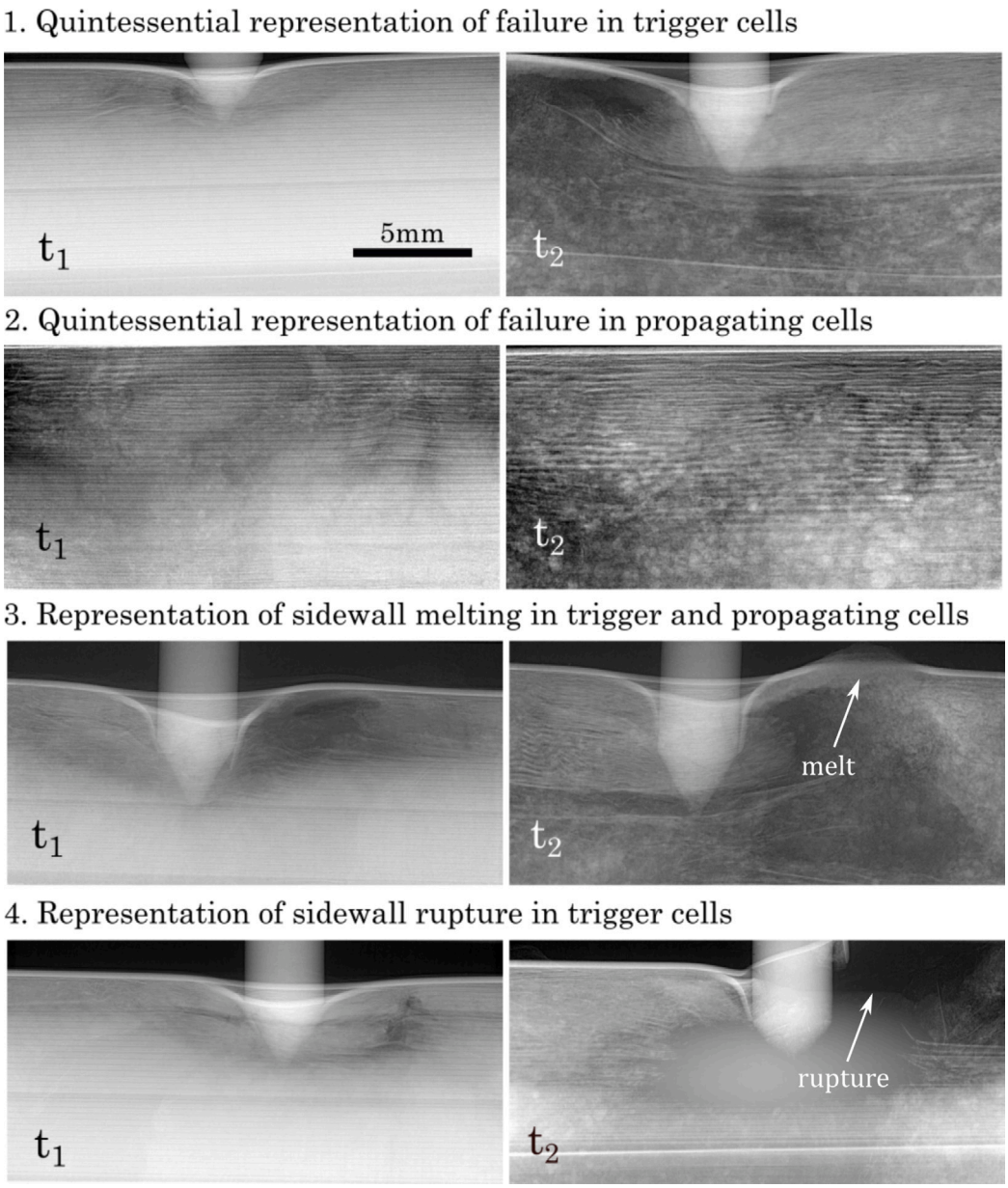

Fig. 2. Selection of images to demonstrate the assigned categories of failures, being: Category 1: Trigger cell failures where cell disintegration initiates to the left of the nail immediately after nail penetration and thereafter spreads within the cell. Category 2: Representation of propagation failures that all exhibit similar dissipation behavior. Category 3: Cases where sidewall melting occurred as a result of TR (trigger and propagating cells) and Category 4: Cases where sidewall rupture occurred as a result of TR (trigger cells).

Measurement data for each conducted experiment, including temperature and propagation time, are presented in tables 1–4, where each experiment has also been assigned to one of the 4 radiography categories. In the end of each column, averages and standard deviations are presented for each data category. Due to movement of cells and thermocouples during failure, some outlier temperature values are still represented in the tables for consistency reasons.

We observe from this data representation that series connection for both P42A and M50 (table 2 and 4) resulted in higher average trigger and propagation cell temperatures than for parallel connected cells (table 1 and 3). This observation can be explained by the electrical current path in the circuit during TR in the trigger cell. When the trigger cell is penetrated in parallel connection and TR initiated, the resistance rapidly decreases, allowing the neighboring cell to be discharged through this cell ('current dumping'), thereby suffering an electrical loss of energy. On the other hand, during TR of the trigger cell in a series circuit, there is no electrical loss of energy, but instead the energy loss is solely thermal, due to the configuration of the connections. This explains the higher temperatures measured for series connection propagation, see Figure 12 Supplementary Materials for illustration.

In Fig. 3(a) it is observed that a minimum of 150 °C is required in the neighboring cell in order for propagation to occur. M50 Parallel shows a slightly lower average propagation onset temperature, however, this temperature is rather equal throughout the groups. The lower temperatures can be correlated to the 'current dumping' occurring in parallel connection (see again Figure 12 in Supplementary Materials), referring to the thermal loss of energy proposed earlier. The onset of TR occurs at a lower temperature for both cell types (P42A and M50) while connected in parallel, and also in a shorter time (see Fig. 3b), and can thus explain the lower measured temperatures as the cell has less time for the TR temperature to build up. This is consistent with series connection, particularly P42A, having the longer average propagation times (Fig. 3a) and reaching the highest temperatures in both trigger

Table 1
Experimental results from P42A Parallel tests, including maximum temperature in both trigger and propagating cell, propagation statistics, time until propagation and assignment to each failure category group.

Experiments P42A	Maximum temperature [°C]		Propagation	Time to propagation [s]	Failure cat.
	Trigger cell	Propagation cell			
P42A_PT_Exp1	723	692	Yes	226	1
P42A_PT_Exp2	289	165	No	–	1
P42A_PT_Exp3	692	502	Yes	464	1
P42A_PT_Exp4	510	468	No	–	3
P42A_PP_Exp1	817	162	No	–	–
P42A_PP_Exp2	725	573	Yes	123	2
P42A_PP_Exp3	816	710	Yes	145	3
P42A_PP_Exp4	813	145	No	–	–
P42A Parallel	$\overline{°C}$ **std**	$\overline{°C}$ **std**	**4/8**	$\bar{s}$ **std**	
	673 185	**427 238**		**240 156**	

Table 2
Experimental results from P42A Series tests, including maximum temperature in both trigger and propagating cell, propagation statistics, time to propagation and assignment to failure category group.

Experiments P42A	Maximum temperature [°C]		Propagation	Time to propagation [s]	Failure cat.
	Trigger cell	Propagation cell			
P42A_ST_Exp1	702	517	Yes	238	4
P42A_ST_Exp2	767	979	Yes	298	1
P42A_ST_Exp3	722	719	No	–	3
P42A_ST_Exp4	800	382	Yes	269	1
P42A_SP_Exp1	535	400	No	–	–
P42A_SP_Exp2	722	142	No	–	–
P42A_SP_Exp3	665	556	Yes	331	2
P42A_SP_Exp4	1172	522	Yes	313	2
P42A Series	$\overline{°C}$ **std**	$\overline{°C}$ **std**	**5/8**	$\bar{s}$ **std**	
	761 184	**527 247**		**290 37**	

and propagating cells. The propagation time is consistently shorter for M50, and appears independent of the type of electrical connection since the difference is less prominent. This is likely due to the chemistry and ratio of active material:electrolyte of the two cell types, which directly affects how easily a TR is initiated. Moreover, no clear trends are observed between sidewall melt/rupture and temperatures or propagation time, and neither is a trend observed in relation to propagation outcome. It is therefore not possible to draw conclusions about sidewall behavior based on the measured parameters.

Heat rate data, calculated as described in the 'Data Processing' section above, shows that propagation occurred in cases with higher heat rates in the neighboring cell, see visually represented in Figure 13(a) in Supplementary Materials. Heat rate data calculated from measured temperatures in Section 2 (see method description Figure 10 in Supplementary Materials) shows that the average heat rate for propagation to occur was 0.4 °C/s compared to 0.1 for non propagating cells and it has been statistically validated that propagation generally occurred in cells experiencing a higher heat rate. However, the heat rate will further depend on the configuration of the cells being tested. For example, in this case, there is no compartment enclosing the two cells, which will allow heat dissipation through the surrounding air. Further in 13(b) in Supplementary Materials, we find that the higher heat rates are also correlated to higher measured temperatures in the propagation cell. The propagation outcome will overall depend on the system and on the specific design, but the data collected in this work can contribute to the meta-model of understanding TR and failure propagation.

Examples of spatio-temporal mapping of X-ray images within each category (as described in the 'Data Processing' section) are presented in Figs. 4 to 7. In each of these figures, (a) – (c) are selected radiographic snapshots from the TR. Image (d) presents the complete spatiotemporal map, and in (e) the ROI that speed mapping has been applied to. Image (f) presents speeds calculated from linear regressions of the lines detected in image (e). To highlight here, the categories are still visually selected and are not based on the retrieved speeds. In Tables 5 and 6, all average speeds for each experiment are presented.

For nail penetration of trigger cells (Category 1) the spatio-temporal map in Figure 4 shows that the electrode layer delamination is initiated to the left of the nail (event 1 in a and e). This is represented by the red area of decorrelation which is appearing here. From thermal images in Figure 14(a)–(c) in Supplementary Materials, it is observed that a large amount of gas and fire is released in this instant. The cell continues to disintegrate in this location for the following 0.4s (event 2 in b and e). The final state of the TR is shown in 4(c) and the thermal state in Figure 14(c) in Supplementary Materials. The maximum speed reached in this example is 0.6 m/s, that in the chosen time frame gradually reached approximately 0.08 m/s as seen in Figure 4(f).

Speed mapping for TR in Category 2 is presented in Fig. 5. In this example, propagation occurred 156 s after TR in the trigger cell. As illustrated in event 1 (a), TR is initiated in the top left corner of the frame. The initiation point is observed as the sections of decorrelation appearing from event 1 and on. The TR then spreads in the top left corner (event 2), and there is a push of layers towards the left of the cell. Compared to the latter case in Category 1, the failure presented here initiates faster, reaching a speed above 25 m/s, however the spreading of the TR is slower and the material exhibits a more dissipating character. The final state is reached in (c) after dissipation of the layers at speeds between 0.01 and 1 m/s. Thermal

Table 3
Experimental results from M50 Parallel tests, including maximum temperature in both trigger and propagating cell, propagation statistics, time to propagation and assignment to failure category group.

Experiments M50	Maximum temperature [°C]				Propagation	Time to propagation [s]		Failure cat.
	Trigger cell		Propagation cell					
M50_PT_Exp1	164		71		No	–		cell movement
M50_PT_Exp2	679		808		No	–		1
M50_PT_Exp3	507		118		No	–		4
M50_PT_Exp4	630		607		Yes	272		4
M50_PP_Exp1	787		381		Yes	152		cell movement
M50_PP_Exp2	644		699		Yes	147		2
M50_PP_Exp3	686		105		No	–		–
M50_PP_Exp4	728		523		Yes	275		2
M50 Parallel	$\overline{°C}$	**std**	$\overline{°C}$	**std**	**4/8**	$\bar{s}$	**std**	
	603	**195**	**414**	**290**		**212**	**72**	

Table 4
Experimental results from M50 Series tests, including maximum temperature in both trigger and propagating cell, propagation statistics, time to propagation and assignment to failure category group.

Experiments M50	Maximum temperature [°C]				Propagation	Time to propagation [s]		Failure cat.
	Trigger cell		Propagation cell					
M50_ST_Exp1	788		128		No	–		1
M50_ST_Exp2	723		133		No	–		4
M50_ST_Exp3	282		763		Yes	177		1
M50_ST_Exp4	756		733		Yes	342		1
M50_SP_Exp1	728		546		Yes	223		2
M50_SP_Exp2	755		698		Yes	149		cell movement
M50_SP_Exp3	832		420		Yes	210		cell movement
M50_SP_Exp4	625		626		No	–		–
M50 Series	$\overline{°C}$	**std**	$\overline{°C}$	**std**	**5/8**	$\bar{s}$	**std**	
	686	**174**	**506**	**256**		**220**	**74**	

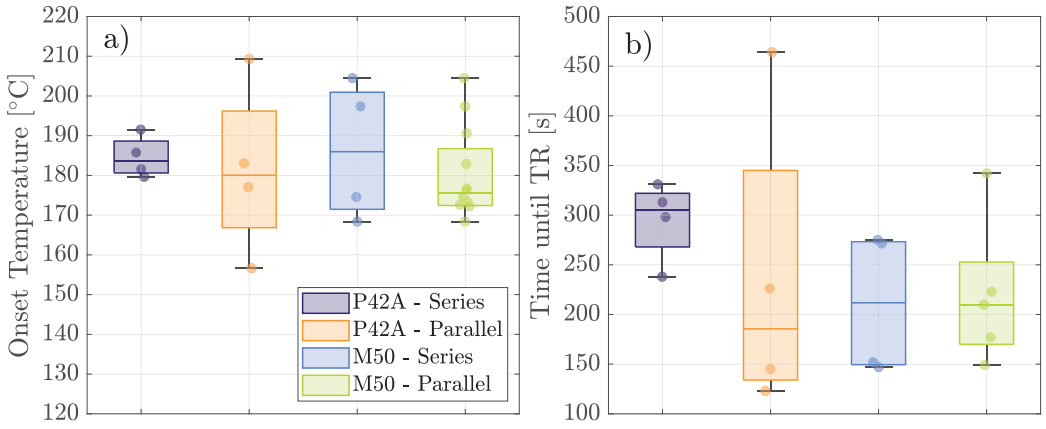

Fig. 3. Box plots showing the distribution of (a) propagation onset temperature and (b) propagation time - for Series, Parallel, P42 A and M50 groups respectively.

images in Figure 14(d) to (f) in Supplementary Materials shows the 'milder' failure process of propagation cells.

Category 3: Fig. 6 illustrates an example of a sidewall melt. In (a) the failure initiation is marked by event 1, which is also marked in the correlation magnitude map in (d) and (e). As the cell is penetrated, fire and gas are ejected from the vent region of the cell as visible in thermal images of Figure 14(g) in Supplementary Materials. The sidewall swelling, melting and the first release of electrode content is shown in event 2 in (b). Fire and gas is continuously violently released (see thermal images in Figure 14(h–i) in Supplementary Materials. The swelling of the sidewall is also visible in the selected ROI in Fig. 6(e) where event 2 marks the deformation of the sidewall leading up to the breaking and ejection of material through the melt. An initiation speed of 2.7 m/s is calculated, which thereafter gradually decreases to 0.14 m/s before the sidewall melt occurred. As visible in the correlation magnitude in Fig. 6(g), after 1.2 s the cell structure is disintegrated to a point where there is no longer any correlation with the original structure.

More severe, pressure driven ruptures of the sidewall is represented in Category 4 (Fig. 7). The point of initiation in a) is to the left of

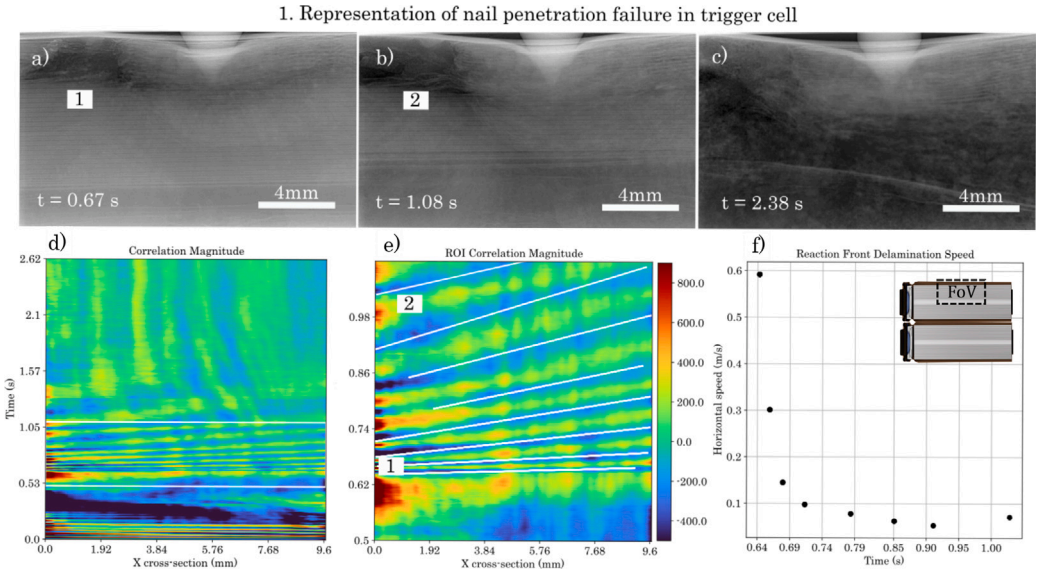

Fig. 4. Spatio-temporal mapping of TR events and speed mapping within ROI-selections in time for Category 1. The figure is composed of a set of sub-images where (a)–(c) are radiography snapshots during TR, (d) the full spatio-temporal mapping of the failure, (e) the selected ROI for speed mapping and (f) speed plot of the TR and a drawing indicating where the FoV is positioned. In (d) and (e), the color bar represents the magnitude of the correlation, where red is strong correlation.

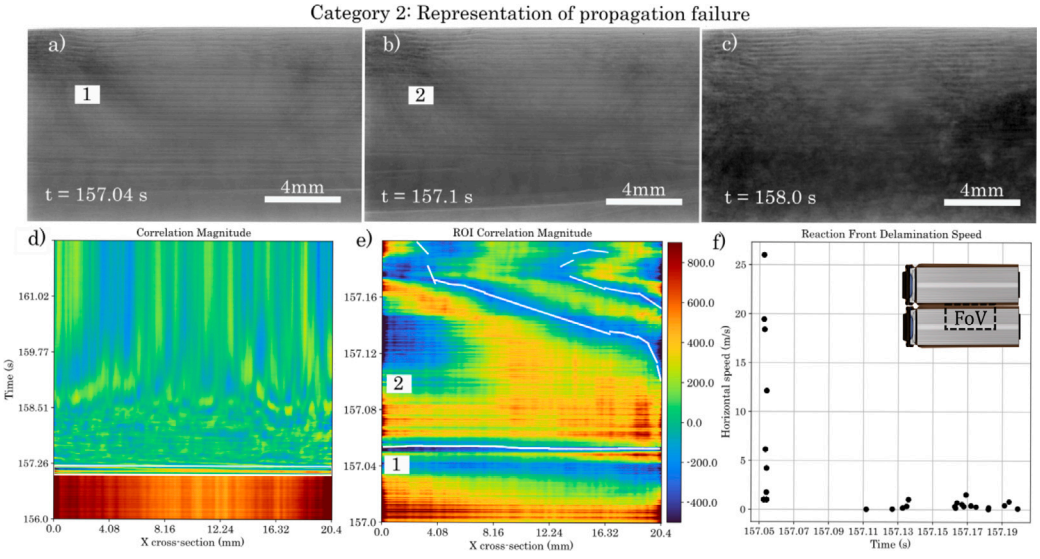

Fig. 5. Event mapping of internal TR events synchronized with the speed representation of ROI-selections in time for Category 2. The figure is composed of a set of sub-images where (a)–(c) are radiography snapshots during TR, (d) the full spatiotemporal mapping of the failure, (e) the selected ROI for speed mapping and (f) speed plot of the event and a drawing indicating where the FoV is positioned. In (d) and (e), the color bar represents the magnitude of the correlation, where red is strong correlation.

the nail and was coupled with a gas and fire release through the vent opening (see 14a) in Supplementary Materials. Shortly afterwards the cell ruptured, as seen by the cell movement that has occurred in event 2 in Fig. 7(b) and (e). The sidewall rupture occurred in 0.27 s, between 10 (b) and (c), and is also visualized in the thermal images in 14(l) in Supplementary Materials. Event 3 in Fig. 7(e) is the end of the cell rupture since due to the large movement of the cell, no correlation is found and thus no speeds can be estimated.

The distribution of 'speed-mapping' values derived for each experiment are presented in Fig. 8, with the maximum delamination velocity and standard deviations for each experiment presented in Tables 5 and 6. In Fig. 8(a)–(c), the distribution of all speeds within the interesting groups trigger/propagation, series/parallel and P42 A series/M50 series groups are presented for each group.

Initially, all speeds in trigger cells are compared to all those in propagating cells, see Fig. 8(a). The two groups are significantly different indicating that propagating cells' internal fails faster than trigger cells. One explanation for the lower speeds for TR in the trigger cells, can be related to the internal heat triggering: in the trigger cells, the failure initiation since this method is mechanically faster with less time for heat build up, whilst in the case of propagation cells, the TR initiates after being heated for a prolonged time, and thus we hypothesize that the TR initiates internal events that are faster due to the elevated global temperature. In Fig. 8(b) the boxplot shows that series-connected TR occur faster than in parallel connection and is also statistically significant. We argue that this can be related to the 'current dumping' process proposed by earlier studies which occur for cells connected in parallel, and once again we have a higher temperature in the series connected cell leading to faster internal TR events. This in accordance with the higher temperature measurements in series connected cells.

It was found that the elapsed time of TR propagation was shorter in M50s, both for parallel and series connection, which is likely to

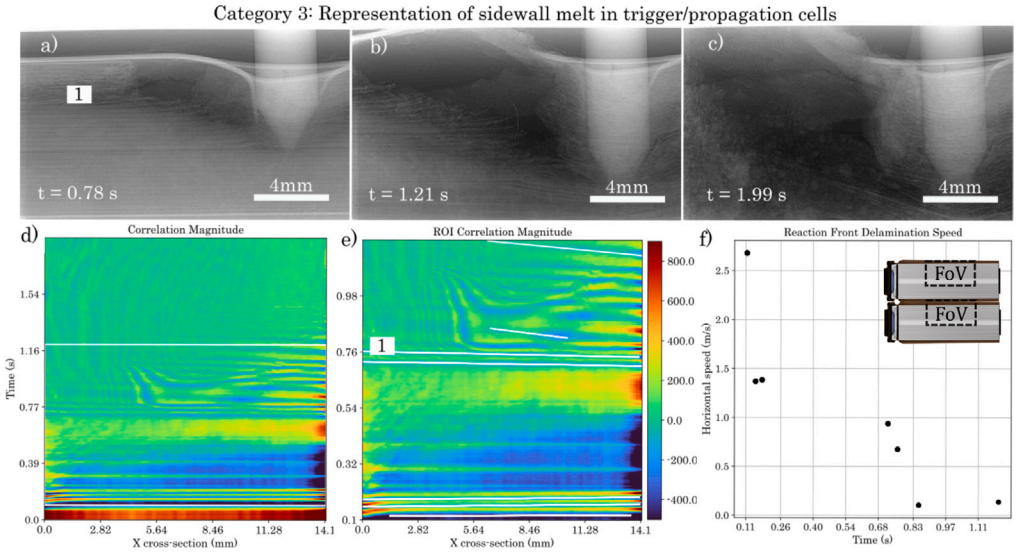

Fig. 6. Event mapping of internal TR events synchronized with the speed representation of ROI- selections in time for Category 3. The figure is composed of a set of sub-images where (a)–(c) are radiography snapshots during TR, (d) the full spatiotemporal mapping of the failure, (e) the selected ROI for speed mapping and (f) speed plot of the event a drawing indicating where the FoV is positioned (both trigger and propagation cells included in this category). In (d) and (e), the color bar represents the magnitude of the correlation, where red is strong correlation.

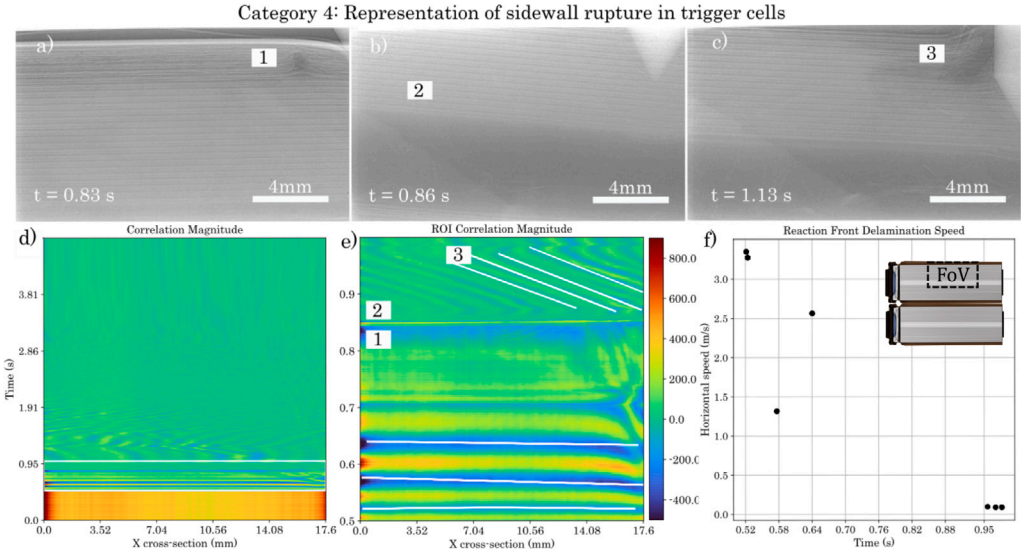

Fig. 7. Event mapping of internal TR events synchronized with the speed representation of ROI-selections in time for Category 4. The figure is composed of a set of sub-images where (a)–(c) are radiography snapshots during TR, (d) the full spatiotemporal mapping of the failure, (e) the selected ROI for speed mapping and (f) speed plot of the event and a drawing indicating where the FoV is positioned. In (d) and (e), the color bar represents the magnitude of the correlation, where red is strong correlation.

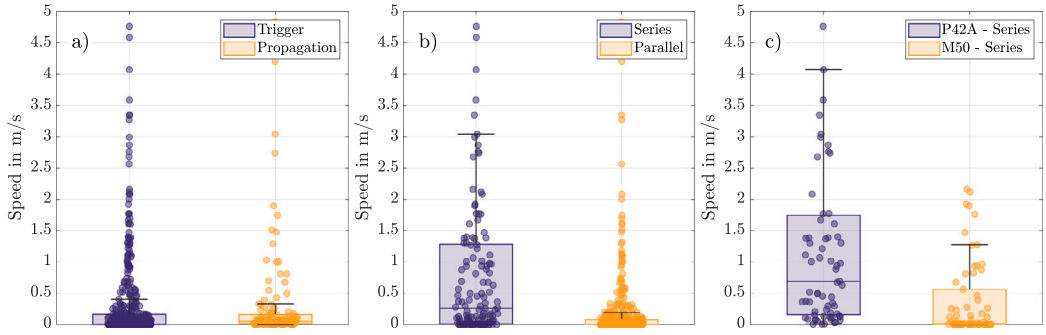

Fig. 8. Box plot comparisons of derived speeds: In (a) Trigger cells vs. Propagating cells, in (b) Series vs. Parallel connected cells and in (c) P42 A series vs. M50 series connection. From the comparisons, it is concluded that P42 A series TR occurs faster than M50 series with a statistical significance.

Table 5
Presentation of average speed values and standard deviations for P42A experiments, derived from Gabor filtering followed by applying ROI segmentation and speed mapping.

Parallel			Series		
Experiments P42A	Maximum speed [m/s]		Experiments P42A	Maximum speed [m/s]	
P42A_PT_Exp1	1.1		P42A_ST_Exp1	0.7	
P42A_PT_Exp2	1.9		P42A_ST_Exp2	7.7	
P42A_PT_Exp3	0.6		P42A_ST_Exp3	2.7	
P42A_PT_Exp4	1.2		P42A_ST_Exp4	6.3	
P42A_PP_Exp2	4.8		P42A_SP_Exp3	3.0	
P42A_PP_Exp3	1.3		P42A_SP_Exp4	12.2	
P42A Parallel	$\bar{v}$	**std**	**P42A Series**	$\bar{v}$	**std**
	1.8	**1.5**		**5.4**	**4.2**

Table 6
Presentation of average speed values and standard deviations for M50 experiments, derived from Gabor filtering followed by applying ROI segmentation and speed mapping.

Parallel			Series		
Experiments M50	Maximum speed [m/s]		Experiments M50	Maximum speed [m/s]	
M50_PT_Exp1	1.7		M50_ST_Exp1	11.6	
M50_PT_Exp2	6.6		M50_ST_Exp2	4.6	
M50_PT_Exp3	24.5		M50_ST_Exp3	1.9	
M50_PT_Exp4	0.7		M50_ST_Exp4	2.1	
M50_PP_Exp1	1.5		M50_SP_Exp1	0.01	
M50_PP_Exp2	12.1		M50_SP_Exp2	1.90	
M50_PP_Exp4	0.17		M50_SP_Exp3	0.81	
M50 Parallel	$\bar{v}$	**std**	**M50 Series**	$\bar{v}$	**std**
	6.8	**8.9**		**3.3**	**3.9**

be chemistry related. Further, the highest average speed is measured for P42As series connection (see Table 5). In Fig. 8(c) all speeds in P42A vs. M50 series configurations are compared and shows that TR in P42 A series occurs faster than the same connection for M50s with statistical significance. The faster failure rate for P42A series can be related to various parameters such as the higher temperatures previously discussed. Another explanation, that simultaneously considers the difference between the two cell models is the differing cell chemistry and internal resistance. A higher internal resistance will lead to a higher temperature, and increased failure rate, such as demonstrated by the results (see also Figure 12(a) for parallel and (b) for series). A greater failure speed decreases the response time, and limits the function of internal safety mechanisms. A higher failure rate additionally leads to lower heat dissipation, which can increase the propagation risk.

5. Conclusion

TR propagation is important to understand in order to design safe battery systems. In the work presented above, we have evaluated the impact of electrical connection and cell chemistry on the risk of cell-to-cell propagation under abusive testing conditions, using high-speed X-ray imaging and additional data analysis. From the results of our tests, we conclude that propagation is not more likely in any of the cases, being the cell model or the electrical connection, but that the overall risk of propagation (56%) is high. Propagation occurred indicatively more often in series connected cells, but not with statistical significance. The propagation time will determine the time for mitigation, and we measured propagation between 123s and 467s. The on average fastest propagation group, M50 series, also measured the highest propagation cell temperature. Furthermore, it was found that the heat rate of neighboring cell has an impact on the propagation outcome.

This work has also shown that higher temperatures are generally reached in series connected cells, due to the increase in internal resistance in the neighboring cell. Composition of active materials and electrolyte will play an important role for temperature generation, as they influence the reaction pathways and hence the exothermic heat release, and is the possible explanation for why P42A series connection experiences higher trigger cell temperatures than M50s.

Sidewall breaches were observed in P42As only, while ruptures only occurred in trigger cells. Sidewall melts in P42A could be chemistry-related and can further be mitigated by separating the cell wall from the active material jellyroll. The pressure-driven ruptures in trigger cells are related to the fast gas accumulation during nail penetration. In this study, the sidewall outcomes did not affect the overall propagation outcome.

Analysis of temperature, X-ray interpretation and speed data has further led to the conclusion that TR occurs faster in series connected cells, and propagating cells, this trend was particularly apparent for P42As. This is partly explained by the cell chemistry having a higher exothermic heat release, thus a higher temperature and following a higher failure rate. Furthermore, the faster failure rate could be correlated to the significantly longer time until TR propagation in P42A Series, meaning that the TR is initiated, the temperature is already higher and thus the electrode delamination occurs faster.

Overall, while designing a safe battery system, there are several parameters to consider, as we have seen that both chemistry and electrical connection impacts the TR evolution. Measured values of temperature and propagation time, as well as derived values for heat rate and speed serves as guidance for focused battery safety research and safety advances. The propagation outcome of 56% should be minimized and we conclude that further research should be conducted to develop high energy, but less thermally sensitive battery materials, where the internal resistance of the cell will play an important role for the evolution of TR. We also conclude that the electrical connections and installation of protection mechanisms such as fuses are crucial for minimizing TR and TR propagation. Results acquired in this work can be used in system models that can aid in the development of better battery safety management systems.

CRediT authorship contribution statement

Matilda Fransson: Writing – original draft, Visualization, Methodology, Formal analysis, Data curation, Conceptualization. **Jonas Pfaff:** Writing – review & editing, Methodology, Formal analysis, Data curation, Conceptualization. **Ludovic Broche:** Writing – review & editing, Supervision, Data curation. **Mark Buckwell:** Writing – review & editing, Methodology, Data curation, Conceptualization. **Charlie Kirchner-Burles:** Methodology, Conceptualization. **Hamish T. Reid:** Methodology, Conceptualization. **Sebastian Schopferer:** Resources, Funding acquisition, Conceptualization. **Alexander Rack:** Supervision, Resources, Project administration, Funding acquisition. **Donal P. Finegan:** Writing – review & editing, Methodology, Conceptualization. **Paul R. Shearing:** Writing – review & editing, Supervision, Resources, Project administration, Funding acquisition, Conceptualization.

Declaration of competing interest

The authors declare that they have no known competing financial interests or personal relationships that could have appeared to influence the work reported in this paper.

Data availability

Data will be made available on request.

Acknowledgments

The authors acknowledge the Faraday Institution's SafeBatt (https://www.safebatt.ac.uk/) project [grant numbers: EP/S003053/1, FIRG028, FIRG059] and the EPSRC, United Kingdom (EP/W003333/1). The Royal Academy of Engineering, United Kingdom is acknowledged for the financial support of PRS and MF (CiET1718/59).

Appendix A. Supplementary data

Supplementary material related to this article can be found online at https://doi.org/10.1016/j.jpowsour.2024.234916.

References

[1] International Energy Agency (IEA)a, Global EV outlook 2022, 2022, https://iea.blob.core.windows.net/assets/ad8fb04c-4f75-42fc-973a-6e54c8a4449a/GlobalElectricVehicleOutlook2022.pdf.

[2] C.P. Grey, D.S. Hall, Prospects for lithium-ion batteries and beyond—a 2030 vision, Nature Commun. 11 (1) (2020) 2–5, http://dx.doi.org/10.1038/s41467-020-19991-4.

[3] International Energy Agency (IEA)b, Grid-scale storage, 2022, https://www.iea.org/reports/grid-scale-storage.

[4] S. Wilke, B. Schweitzer, S. Khateeb, S. Al-Hallaj, Preventing thermal runaway propagation in lithium ion battery packs using a phase change composite material: An experimental study, J. Power Sources 340 (2017) 51–59, http://dx.doi.org/10.1016/j.jpowsour.2016.11.018, URL http://dx.doi.org/10.1016/j.jpowsour.2016.11.018.

[5] D.P. Finegan, M. Scheel, J.B. Robinson, B. Tjaden, I. Hunt, T.J. Mason, J. Millichamp, M. Di Michiel, G.J. Offer, G. Hinds, D.J. Brett, P.R. Shearing, In-operando high-speed tomography of lithium-ion batteries during thermal runaway, Nature Commun. 6 (2015) 1–10, http://dx.doi.org/10.1038/ncomms7924.

[6] D.P. Finegan, B. Tjaden, T. M.M. Heenan, R. Jervis, M.D. Michiel, A. Rack, G. Hinds, D.J.L. Brett, P.R. Shearing, Tracking internal temperature and structural dynamics during nail penetration of lithium-ion cells, J. Electrochem. Soc. 164 (13) (2017) A3285–A3291, http://dx.doi.org/10.1149/2.1501713jes.

[7] L. Kong, C. Li, J. Jiang, M.G. Pecht, Li-ion battery fire hazards and safety strategies, Energies 11 (9) (2018) 1–11, http://dx.doi.org/10.3390/en11092191.

[8] B. Mao, H. Chen, Z. Cui, T. Wu, Q. Wang, Failure mechanism of the lithium ion battery during nail penetration, Int. J. Heat Mass Transfer 122 (2018) 1103–1115, http://dx.doi.org/10.1016/j.ijheatmasstransfer.2018.02.036, URL https://doi.org/10.1016/j.ijheatmasstransfer.2018.02.036.

[9] X. Feng, M. Ouyang, X. Liu, L. Lu, Y. Xia, X. He, Thermal runaway mechanism of lithium ion battery for electric vehicles: A review, Energy Storage Mater. 10 (May 2017) (2018) 246–267, http://dx.doi.org/10.1016/j.ensm.2017.05.013.

[10] J. Duan, X. Tang, H. Dai, Y. Yang, W. Wu, X. Wei, Y. Huang, Building safe lithium-ion batteries for electric vehicles: A review, Electrochemical Energy Reviews, vol. 3, (1) Springer Singapore, 2020, pp. 1–42, http://dx.doi.org/10.1007/s41918-019-00060-4.

[11] S. Ma, M. Jiang, P. Tao, C. Song, J. Wu, J. Wang, T. Deng, W. Shang, Temperature effect and thermal impact in lithium-ion batteries: A review, Progress in Natural Science: Materials International 28 (6) (2018) 653–666, http://dx.doi.org/10.1016/j.pnsc.2018.11.002.

[12] C. Xu, F. Zhang, X. Feng, F. Jiang, D. Ren, L. Lu, Y. Yang, G. Liu, X. Han, B. Friess, M. Ouyang, Experimental study on thermal runaway propagation of lithium-ion battery modules with different parallel-series hybrid connections, J. Clean. Prod. 284 (2021) 124749, http://dx.doi.org/10.1016/j.jclepro.2020.124749.

[13] J. Lamb, C.J. Orendorff, L.A.M. Steele, S.W. Spangler, Failure propagation in multi-cell lithium ion batteries, J. Power Sources 283 (2015) 517–523, http://dx.doi.org/10.1016/j.jpowsour.2014.10.081, URL http://dx.doi.org/10.1016/j.jpowsour.2014.10.081.

[14] C.F. Lopez, J.A. Jeevarajan, P.P. Mukherjee, Experimental analysis of thermal runaway and propagation in lithium-ion battery modules, J. Electrochem. Soc. 162 (9) (2015) A1905–A1915, http://dx.doi.org/10.1149/2.0921509jes.

[15] R. Srinivasan, M.E. Thomas, M.B. Airola, B.G. Carkhuff, L.J. Frizzell-Makowski, H. Alkandry, J.G. Reuster, H.N. Oguz, P.W. Green, J. La Favors, L.J. Currano, P.A. Demirev, Preventing cell-to-cell propagation of thermal runaway in lithium-ion batteries, J. Electrochem. Soc. 167 (2) (2020) 020559, http://dx.doi.org/10.1149/1945-7111/ab6ff0.

[16] S.T. Plunkett, C. Chen, R. Rojaee, P. Doherty, Y. Sik Oh, Y. Galazutdinova, M. Krishnamurthy, S. Al-Hallaj, Enhancing thermal safety in lithium-ion battery packs through parallel cell 'current dumping' mitigation, Appl. Energy 286 (January) (2021) 116495, http://dx.doi.org/10.1016/j.apenergy.2021.116495.

[17] T. Liu, J. Hu, C. Tao, X. Zhu, X. Wang, Effect of parallel connection on 18650-type lithium ion battery thermal runaway propagation and active cooling prevention with water mist, Appl. Therm. Eng. 184 (November 2020) (2021) 116291, http://dx.doi.org/10.1016/j.applthermaleng.2020.116291.

[18] B. Mao, H. Chen, Z. Cui, T. Wu, Q. Wang, Failure mechanism of the lithium ion battery during nail penetration, Int. J. Heat Mass Transfer 122 (2018) 1103–1115, http://dx.doi.org/10.1016/j.ijheatmasstransfer.2018.02.036, URL https://www.sciencedirect.com/science/article/pii/S0017931017342606.

[19] J. Pfaff, M. Fransson, L. Broche, M. Buckwell, D.P. Finegan, S. Moser, S. Schopferer, S. Nau, P.R. Shearing, A. Rack, In situ chamber for studying battery failure using high-speed synchrotron radiography research papers, J. Synchrotron Radiat., 2023, pp. 1–8, http://dx.doi.org/10.1107/S1600577522010244.

[20] M. Fransson, L. Broche, M. Buckwell, J. Pfaff, H. Reid, C. Kirchner-Burles, M. Pham, S. Moser, A. Rack, S. Nau, S. Schopferer, D. Finegan, P. Shearing, Sidewall breach during lithium-ion battery thermal runaway triggered by cell-to-cell propagation visualized using high-speed X-ray imaging, J. Energy Storage 71 (2023) http://dx.doi.org/10.1016/j.est.2023.108088.

[21] M. Fransson, L. Broche, GitHub - matildafransson/GaborSpeedMap: Code to retrieve speed from patterns in spatio-temporal map from gabor filtering + cross correlation — github.com, https://github.com/matildafransson/GaborSpeedMap, (Accessed 1 May 2024).

[22] A.N. Radhakrishnan, M. Buckwell, M. Pham, D.P. Finegan, A. Rack, G. Hinds, D.J. Brett, P.R. Shearing, Quantitative spatiotemporal mapping of thermal runaway propagation rates in lithium-ion cells using cross-correlated Gabor filtering, Energy Environ. Sci. 15 (8) (2022) 3503–3518, http://dx.doi.org/10.1039/d1ee03430h.